

Collisional-radiative study of lithium plasmasS. D. Loch,¹ C. J. Fontes,² J. Colgan,¹ M. S. Pindzola,¹ C. P. Ballance,³
D. C. Griffin,³ M. G. O'Mullane,⁴ and H. P. Summers⁴¹*Department of Physics, Auburn University, Auburn, Alabama 36849, USA*²*Los Alamos National Laboratory, MS F663, Los Alamos, New Mexico 87545, USA*³*Department of Physics, Rollins College, Winter Park, Florida 32789, USA*⁴*Department of Physics, University of Strathclyde, Glasgow, G4 0NG, United Kingdom*

(Received 1 December 2003; published 4 June 2004)

The sensitivity of lithium plasma models to the underlying atomic data is investigated. Collisional-radiative modeling is carried out with both the Los Alamos and ADAS suite of codes. The effects of plane-wave Born, distorted-wave, and nonperturbative R -matrix with pseudostates and time-dependent close-coupling electron impact atomic data on derived plasma quantities such as the ionization balance and radiated power are studied. Density and temperature regimes are identified where nonperturbative excitation and ionization rate coefficients must be used. The electron temperature and density ranges investigated were $0.2 \text{ eV} \leq T_e \leq 90 \text{ eV}$ and $10^{10} \text{ cm}^{-3} \leq N_e \leq 10^{14} \text{ cm}^{-3}$.

DOI: 10.1103/PhysRevE.69.066405

PACS number(s): 52.25.Dg, 52.20.Fs, 34.80.Dp

I. INTRODUCTION

The amount and quality of fundamental atomic data made available to the plasma modeling community continues to increase, as is shown by the number and breadth of atomic databases now present [1–3]. As new data are calculated or measured, comparisons are typically provided among these fundamental results (i.e., cross sections or rate coefficients) in order to discern similarities, differences, the need for better experiments or calculations, etc. However, a comparison of the effects that these data might have on modeling calculations is less often undertaken for a number of reasons. For example, it is difficult to gather a complete set of data, for a given ion, which is necessary to carry out a collisional-radiative modeling calculation. Sometimes data are available for only a few ion stages of a particular species, or, if all ion stages are represented, the data may not cover a sufficient range of physical parameter space (e.g., electron impact energy, photon energy, plasma temperature or density, etc.) to carry out a detailed collisional-radiative study. Additionally, once the data are gathered, it is often not in a single, convenient format for collisional-radiative modeling calculations. A significant amount of time and effort can be expended in order to augment large amounts of data so that they can be incorporated into a consistent modeling calculation.

The purpose of this work is of a twofold nature: (1) to demonstrate the usefulness of combining two well-established collisional-radiative modeling efforts—namely, the Atomic Data and Analysis Structure (ADAS) [2] and Los Alamos National Laboratory (LANL) [4] suites of codes—and (2) to apply this approach to a specific atomic species, lithium in this case, in order to determine the sensitivity of measurable plasma quantities to various sets of atomic data. For this study we have chosen lithium for a number of reasons. It has proved to be very successful in neutral beam diagnostics of magnetic fusion energy (MFE) plasmas; see, for example, the work of Brandenburg *et al.* [5]. Also, the small number of ion stages allows for a relatively compact atomic model, producing a simple enough system to allow a

detailed understanding of the similarities and differences produced by the two collisional-radiative models.

To date a significant amount of lithium data has been produced. In particular recent efforts on atomic data calculations for lithium have produced an atomic database which is both relatively complete and consists of data for which one can have a high degree of confidence in its accuracy. The new data consist of electron impact excitation data [6–8] and ionization [9,10] and dielectronic recombination data [11]. This allows us to compare the results from more approximate fundamental data sets with those produced from the best atomic data available. The outcome of these comparisons is very useful in determining when computer-intensive, nonperturbative data are required versus more approximate data that can be computed with less effort.

Various collisional-radiative modeling papers on lithium have been published. The papers of Kawachi, Fujimoto, and Csanak [12] and Kawachi and Fujimoto [13] describe a collisional-radiative model for lithiumlike plasmas. The underlying atomic data are taken from the Los Alamos suite of codes, as well as from analytic formulae for high-lying levels. This work was recently extended to include the effects of doubly excited configurations; see the paper of Kawachi [14]. The work of Brandenburg *et al.* [5] describes the results of a collisional-radiative model for lithium beam studies. The atomic data for this work are taken from Schweinzer *et al.* [15] and contain nonperturbative data for the electron impact excitation and ionization rate coefficients. The database of Schweinzer *et al.* also contains considerable proton impact data due to the relevance of that work to lithium beam diagnostics. The present study concentrates on the influence of the electron impact data on lithium modeling, and does not look at the sensitivity of plasma models to the underlying proton collisional data.

II. DESCRIPTION OF THE COLLISIONAL-RADIATIVE CODES

The two modeling efforts that shall be discussed are that of the ADAS codes [2,16] and that from the atomic data

codes of the Los Alamos National Laboratory [4]. Both codes solve the set of collisional-radiative equations which determine the populations of the emitting ions in a plasma. However, the codes use different approaches, which will be discussed shortly. These equations consist of a set of time-dependent differential equations with one equation for each level i in every ion stage of the model. That is,

$$\frac{dN_i}{dt} = \sum_j C_{ij}N_j, \quad (1)$$

where N_i is the number density of a given level and the summation on the right-hand side extends over all levels of all ion stages. The terms in the collisional-radiative matrix C_{ij} represent the contributions from all collisional and radiative processes (i.e., collisional excitation and deexcitation, collisional ionization and three-body recombination, autoionization and dielectronic capture, photoexcitation and radiative decay, and photoionization and radiative recombination).

The LANL codes originate from an inertial fusion environment and thus typically deal with highly ionized species at higher densities and temperatures than the ADAS codes. The LANL suite consists of the CATS, ACE, GIPPER, and FINE codes [4]. The first three codes are used to compute the fundamental atomic data, such as wave functions, oscillator strengths, cross sections, etc., which are necessary to solve the rate equations. The FINE code uses these fundamental data to compute rate coefficients, solves for the populations, and synthesizes spectra from these results. Note that these codes can work at various levels of refinement which include configuration average, term average, and fine structure calculations. Due to the relative simplicity of lithium, it was possible to compute a fine structure model for the present study.

In solving for the level populations the LANL codes assemble a single C_{ij} rate matrix, containing all possible transitions within an ion stage, as well as between levels in adjacent ion stages. That is, all of the level populations, among all of the ion stages, are solved for simultaneously from the set of coupled rate equations. The FINE code treats all levels explicitly, including high- n -shell and autoionizing levels. So there is allowance for population to actually reside in these high-lying levels. The LANL approach involves the inclusion of progressively more n shells until the population calculation converges. The LANL codes have the capability to either keep all of the time dependence in the solution of the system of equations represented by Eq. (1) or to set all of the time derivatives to zero and return the full equilibrium (i.e., steady-state) solution. In providing the present comparisons between the LANL and ADAS codes we have chosen to present results for the full equilibrium case.

The LANL suite can calculate the atomic cross sections within various physical approximations. It was decided to choose a very basic model and a more accurate model in order to highlight the effects of the quality of the atomic data on the modeling results. The basic model uses plane-wave Born collisional excitation data and scaled hydrogenic collisional ionization data [17], which will be referred to as LANL-PWB. The more accurate model uses distorted-wave

data for both of these collisional processes and will be referred to as LANL-DW. In both of these models, the distorted-wave approach was used to compute the continuum electron wave functions needed for autoionization and photoionization processes, as these cross sections require significantly less computational effort than the collisional results. Note that the distorted-wave data are the most accurate that can be computed by the LANL codes, as opposed to ADAS, which can utilize the more accurate nonperturbative [R -matrix with pseudostates (RMPS), time-dependent close-coupling (TDCC), and convergent close coupling (CCC)] data.

The ADAS codes grew out of the magnetically confined fusion community and are primarily concerned with optically thin plasmas over temperature and density ranges encountered in magnetically confined tokamak devices, though it is also in wide use in astrophysical studies. The focus of the ADAS project has been largely on light elements, though its scope is currently being extended to heavier species. As with the LANL suite, the ADAS codes can work at configuration average, term, or level resolution (or, more generally, at whatever resolution the atomic data have been archived). The lithium results for this paper were all calculated at term resolution.

The ADAS codes make the assumption of quasistatic equilibrium when determining a solution to the collisional-radiative equations. This assumption naturally divides the levels into two categories: the metastable levels (including the ground state) that are relatively long lived and the excited levels, which comprise the remaining levels. Physically, the quasistatic approach means that the excited level populations within an ion stage are considered to be in instantaneous equilibrium with the metastable levels of the element under consideration. The metastables are assumed to contain a large majority of the population within a given ion stage and so a determination of these populations will provide the ionization balance of the system. On the other hand, a determination of the excited level populations is required for spectral quantities, such as the radiated power loss.

Mathematically, this approach requires that the time derivatives for all of the excited level populations in Eq. (1) be set to zero, while those for the metastables must be solved directly. The result is a system of equations that is divided into two pieces: the ionization balance calculation, which determines the metastable populations, and the excited level population calculation, which requires as input the metastable populations from the previous calculation. The ADAS codes can be used to solve explicitly for these time-dependent metastable populations, or they can be taken in from other codes, such as plasma transport codes. The excited populations may then be obtained from these data at each time interval for which the metastable populations have been provided.

For the particular case of full equilibrium being considered in this work [i.e., dN/dt for all of the metastable levels is set to zero in Eq. (1)], we provide the equations that are solved by the ADAS codes in order to compare with the LANL approach as well as to facilitate the discussion of results that follows. We define the following notation for the ADAS formalism: the metastable levels are denoted by

Greek letter subscripts and excited levels are denoted by Roman letter subscripts. Specifically, the metastables of ion stage z are denoted by the set σ . The metastable levels of the $z+1$ ion stage are denoted by ν , and μ denotes metastable levels of the $z-1$ stage. ADAS assembles the collisional-radiative matrix \mathcal{C} for ion stage z involving rates from metastable to excited levels $\mathcal{C}_{i\sigma}$, rates between excited levels \mathcal{C}_{ji} , and rates between metastable levels $\mathcal{C}_{\sigma\sigma'}$. Recombination rate coefficients \mathcal{R} and ionization rate coefficients \mathcal{S} can appear both explicitly and embedded in \mathcal{C} -matrix elements. For example, $\mathcal{R}_{i\nu}$ gives the recombination rate coefficient from level ν of the $z+1$ ion stage, and $\mathcal{S}_{i\mu}$ gives the collisional ionization rate coefficient from level μ of ion stage $z-1$, into level i of ion stage z . These matrix elements and rate coefficients are then used to solve for the metastable and excited level populations.

When solving for the ionization balance of a system, one can solve for the ion-stage populations or for the metastable populations within each ion stage. The first instance is called the “unresolved” case and the second the metastable “resolved” case. While ADAS is typically used to solve the resolved case, it is useful to first describe the unresolved case. As will be shown in the upcoming comparisons section, a set of unresolved rate coefficients can be extracted from the LANL calculations and compared directly with those used in the ADAS calculation. For each of these cases one can define effective rate coefficients connecting the various ion stages or metastable levels.

In the unresolved case, the ionization balance equation takes the form

$$\frac{dN_\sigma^z}{dt} = N_e S^{(z-1 \rightarrow z)} N_\sigma^{z-1} - N_e (S^{(z \rightarrow z+1)} + \alpha^{(z \rightarrow z-1)}) N_\sigma^z + N_e \alpha^{(z+1 \rightarrow z)} N_\sigma^{z+1}, \quad (2)$$

where one of these equations exists for each ion stage. The (unresolved) effective ionization rate coefficient S and effective recombination rate coefficient α are defined by

$$\alpha^{(z+1 \rightarrow z)} = \sum_{i,j} \frac{N_j^{z+1}}{N_\sigma^{z+1}} \mathcal{R}_{ij} \quad (3)$$

and

$$S^{(z \rightarrow z+1)} = \sum_{i,j} \frac{N_i^z}{N_\sigma^z} \mathcal{S}_{ji}, \quad (4)$$

where the index i is summed over all levels in ion stage z and similarly for index j over all levels of ion stage $z+1$. [Note that, in this case only, the Roman indices in Eqs. (3) and (4) represent *both* metastable and excited levels.] Thus these unresolved effective coefficients account for ionization and recombination originating from all levels of a given ion stage and terminating in all possible levels of the adjacent stages.

In the case of the metastable resolved ionization balance equation, there exist coupling terms between metastables of the same ion stage, in addition to (resolved) effective ionization and recombination rate coefficients. If one neglects ion-

ization to, and recombination from, excited levels, then the resolved ionization balance equation can be written in the form

$$\begin{aligned} \frac{dN_\sigma^z}{dt} = & N_e \sum_\mu S_{\mu \rightarrow \sigma} N_\mu^{z-1} - N_e \left(\sum_\mu \alpha_{\sigma \rightarrow \mu} + \sum_\nu S_{\sigma \rightarrow \nu} \right. \\ & \left. + \sum_{\sigma'} Q_{\sigma \rightarrow \sigma'} + \sum_{\sigma'} X_{\sigma \rightarrow \sigma'} \right) N_\sigma^z + N_e \sum_\nu \alpha_{\nu \rightarrow \sigma} N_\nu^{z+1} \\ & + N_e \left(\sum_{\sigma'} Q_{\sigma' \rightarrow \sigma} + \sum_{\sigma'} X_{\sigma' \rightarrow \sigma} \right) N_{\sigma'}^z, \end{aligned} \quad (5)$$

where there exists one of these equations for each metastable level. The neglect of these ionization and recombination processes is expected to be valid when modeling low-density plasmas such as those relevant for MFE applications. The quantity $S_{\sigma \rightarrow \nu}$ is the (resolved) effective ionization rate coefficient from metastable $\sigma \rightarrow \nu$ and $\alpha_{\nu \rightarrow \sigma}$ is the (resolved) effective recombination rate coefficient from $\nu \rightarrow \sigma$. Here Q and X represent metastable cross-coupling rate coefficients that connect metastable levels with the same ion stage. These quantities have the definitions

$$\alpha_{\nu \rightarrow \sigma} = \mathcal{R}_{\sigma\nu} - \sum_{j=1}^o \mathcal{C}_{\sigma j} \sum_{i=1}^o \mathcal{C}_{ji}^{-1} \mathcal{R}_{i\nu}, \quad (6)$$

$$S_{\sigma \rightarrow \nu} = \mathcal{S}_{\nu\sigma} - \sum_{j=1}^o \mathcal{S}_{\nu j} \sum_{i=1}^o \mathcal{C}_{ji}^{-1} \mathcal{C}_{i\sigma}, \quad (7)$$

$$Q_{\sigma \rightarrow \sigma'} = N_e \sum_{j=1}^o \mathcal{S}_{\sigma' j} \sum_{i=1}^o \mathcal{C}_{ji}^{-1} \mathcal{R}_{i\sigma}, \quad (8)$$

and

$$X_{\sigma \rightarrow \sigma'} = \left(\mathcal{C}_{\sigma'\sigma} - \sum_{j=1}^o \mathcal{C}_{\sigma' j} \sum_{i=1}^o \mathcal{C}_{ji}^{-1} \mathcal{C}_{i\sigma} \right) / N_e, \quad (9)$$

where the summations are over all the excited levels o in the appropriate ion stage. These cross-coupling and effective rate coefficients are tabulated on an electron temperature/density grid and are particularly useful in modeling impurity plasma transport. The archiving of these rate coefficients allows them to be obtained over a range of plasma conditions via interpolation, providing a quick solution to the ionization balance equations. This is to be contrasted with the LANL method which builds a new rate matrix at each temperature/density point before solving the resulting system of equations. Collisional-radiative coefficients were first introduced by Bates, Kingston, and McWhirter [18] in their formulation of the collisional-radiative modeling of optically thin plasmas. Their “collisional-recombination coefficient” was later extended by Burgess and Summers [19] to include the effects of dielectronic recombination and was termed a “collisional-dielectronic recombination coefficient.” Other notable work in the area of effective rate coefficients is the work of Jacobs and Davis [20], who included the effects of angular redistribution among the autoionizing levels. Jacobs and Davis

found that due to the effects of multiple collisional excitations on the populations of the highly excited bound levels of the recombining ion, the collisional-dielectronic recombination rate coefficients can be reduced by about an order of magnitude from their coronal model values. They also found that collisionally induced angular momentum redistribution among the populations of the autoionizing levels could significantly increase the dielectronic recombination rates into the highly excited bound levels. Recently Badnell *et al.* [11] demonstrated that the Burgess-Bethe general program (BBGP) could be used to model the l redistribution of doubly excited states and used as a correction to more accurate, but undistributed, dielectronic data.

Assuming full equilibrium conditions, the metastable populations are obtained by solving the system of coupled linear equations that result when the time derivatives are set to zero in Eq. (5). The metastable populations, along with the rate matrix and ionization and recombination rate coefficients, can then be used to obtain the excited-level populations N_j via the formula

$$\begin{aligned}
 N_j^z = & - \sum_i C_{ji}^{-1} \sum_{\sigma} C_{i\sigma} N_{\sigma}^z + N_e \sum_i C_{ji}^{-1} \sum_{\nu} \mathcal{R}_{i\nu} N_{\nu}^{z+1} \\
 & + N_e \sum_i C_{ji}^{-1} \sum_{\mu} \mathcal{S}_{i\mu} N_{\mu}^{z-1} \equiv \sum_{\sigma} F_{j\sigma}^{(ex)} N_e N_{\sigma}^z \\
 & + \sum_{\nu} F_{j\nu}^{(rec)} N_e N_{\nu}^{z+1} + \sum_{\mu} F_{j\mu}^{(ion)} N_e N_{\mu}^{z-1}, \quad (10)
 \end{aligned}$$

where the excited population has been split into contributions arising from excitation, recombination, and ionization. Note that the excited populations are obtained from a simple algebraic evaluation of Eq. (10) rather than from a (more time-consuming) solution of the complete system of coupled equations. Of course, the C_{ji}^{-1} matrix elements in Eq. (10) must be obtained by solving a smaller system of coupled equations, involving only the excited-level rate equations.

Typically ADAS contains high quality atomic data only for n shells up to about $n=4$ or 5. The effect on these ‘‘spectroscopic’’ levels due to the influence of the higher states is included through the use of a ‘‘projection matrix.’’ This projection matrix contains an archive of the condensed, more approximate, rate coefficients from all the higher states onto the lower spectroscopic levels. The projection matrix typically includes n shells up to $n=500$. ADAS computes populations for the spectroscopic levels, in order to generate various physical quantities. Populations for the higher-lying projection matrix levels are typically ignored for this purpose, although they could be generated via Eq. (10) if necessary.

When comparing results between the LANL and ADAS codes it was decided to examine the standard quantities of ionization balance and radiated power loss (RPL). The ionization balance, or ion fraction abundance, f^z for ion stage z is given by

$$f_{\text{LANL}}^z = \sum_i N_i^z / N_{\text{tot}} \quad \text{or} \quad f_{\text{ADAS}}^z = \sum_{\sigma} N_{\sigma}^z / N_{\text{tot}}, \quad (11)$$

where the LANL summation is over all levels within the ion stage z and the ADAS summation is over all metastable lev-

els within the ion stage. In both expressions the total ion number density is denoted by N_{tot} . Given identical sets of atomic data, the two methods should produce identical ion fractions, provided that a sufficient number of metastable levels has been defined in the ADAS calculation. The radiated power loss

$$\text{RPL}(T_e, N_e) = \sum_z \sum_{jk} A_{j \rightarrow k}^z \Delta E_{jk}^z \frac{N_j^z}{N_e N_{\text{tot}}} \quad (12)$$

requires the spontaneous emission rates $A_{j \rightarrow k}^z$ along with the corresponding transition energy ΔE_{jk}^z and excited-level population. Note that ADAS assembles this last quantity from the excited and recombining contributions to N_j^z (the ionizing part is usually negligible for MFE plasmas) according to how many metastable levels have been defined [see Eq. (10)], whereas the LANL approach returns a complete value of N_j^z directly from the solution of the full rate matrix. Also of note is that only the bound-bound contribution to the radiated power loss has been included in the present calculations. The bound-free (radiative recombination) and free-free (bremsstrahlung) contributions were found to be negligible over most of the range of physical conditions considered. The only exception was the bound-free contribution to the radiated power loss from neutral lithium at the highest density $N_e = 10^{14} \text{ cm}^{-3}$ at temperatures of $T_e \geq 1.0 \text{ eV}$. This exception will be mentioned explicitly in the forthcoming discussion.

Ideally we would like to compare the best LANL and best ADAS calculations, and from there determine any sensitivity to the underlying atomic data in each of the models. However, it is difficult to ascertain whether differences in the results are due to differences in the underlying data or differences in the methods employed in the solution of the collisional-radiative equations.

There are four significant differences between the LANL and ADAS approaches that must be considered. First there is the difference associated with solving the complete set of collisional-radiative equations versus a decomposition into metastable and excited levels. These two approaches have been described in detail and they cannot be altered, as they are fundamental to the LANL and ADAS formalisms. A second difference occurs in the handling of the highly excited levels. The LANL codes typically model excited levels with higher- n shells (up to $n=8$ in this work), whereas ADAS models spectroscopic levels with n shells up to about $n=4$ or 5. However, as mentioned earlier, ADAS has the additional capability of including the effects of higher excited levels (up to $n=500$) via a projection matrix. A third difference involves the treatment of the autoionizing levels. The LANL codes treat the autoionizing levels explicitly, on the same par as the bound levels, allowing all possible transitions among these levels, as well as transitions between them and a bound level. The ADAS codes include the effects of the autoionizing levels implicitly, to the extent that they are included in the fundamental cross sections or rates that describe transitions between the explicit, spectroscopic levels. An example of this implicit treatment would be the inclusion of resonances in the collisional excitation cross sections of an R -matrix calculation. ADAS does include some autoionizing

TABLE I. Description of LANL and ADAS calculations.

Name	Description
LANL-1	Standard LANL calculation, but all autoionizing levels are excluded
ADAS-1	Standard ADAS calculation, but the projection matrix is turned off
LANL-2	Standard LANL calculation (including autoionizing levels)
ADAS-2	Standard ADAS calculation (including the projection matrix)

configurations within the projection matrix, though for the data presented here, l redistribution among the autoionizing levels has not been included, since its effects are expected to be small at the densities investigated. As mentioned in connection with Eq. (5), the fourth difference is that ADAS typically ignores ionization to, and recombination from, excited (i.e., nonmetastable) levels. This approximation is expected to be valid for the low-density plasmas under consideration in this work and will be mentioned to a limited extent in the comparisons of the next section. Despite these differences it is still possible to isolate the sensitivity due to the underlying data in the two codes. In order to achieve this goal the ADAS and LANL codes were run in two separate modes. One mode allowed a direct comparison between the codes by using nearly identical data sets in the modeling calculations. The other mode represents the highest quality and most physically meaningful calculation that each code can provide.

More specifically, the direct comparison calculations were carried out with the following omissions (see Table I for details). The LANL calculations, denoted by LANL-1, ex-

clude all autoionizing levels. The ADAS calculations, denoted by ADAS-1, exclude the projection matrix. Furthermore, each calculation uses the same data set, the LANL-DW model (see Table II for details). Thus, both the LANL-1 and ADAS-1 calculations include explicit bound (or spectroscopic) levels up to $n=8$, and all of the cross section data connecting these levels were computed by the LANL codes in the distorted-wave approximation. In order to use these LANL-DW results in the ADAS codes we developed a method whereby a significant portion of the LANL data (excluding ionization to, and recombination from, excited levels) can be imported into the ADAS database. These calculations allow us to compare the ADAS and LANL approaches for solving the collisional-radiative equations with essentially the same atomic data in each calculation. If the populations from these two calculations agree, then we have some confidence that the two collisional-radiative approaches are equivalent for the parameter space under investigation.

For the physically meaningful comparisons, a more accurate LANL-2 calculation was carried out, which included autoionizing levels. Similarly, an ADAS-2 calculation was performed with the projection matrix included. This calculation explicitly treated spectroscopic levels up to $n=4$ or 5, while the projection matrix was used to compute the effects of higher-lying excited levels. The LANL-2 calculation was performed with both the LANL-PWB and LANL-DW data sets. These LANL-DW results represent the highest-quality calculation that the LANL codes can provide. The ADAS-2 calculation was performed with the ADAS-NP (nonperturbative) data set, which includes nonperturbative excitation and ionization data. These ADAS-NP results represent the best calculation that ADAS can provide. Table II gives more details concerning these various data sets.

TABLE II. Description of LANL and ADAS data sets.

Name	Description
LANL-PWB	Data computed by LANL codes. Levels up to $n=8$, PWB collisional excitation data, scaled hydrogenic collisional ionization data, DW continuum orbitals used in calculating radiative recombination and autoionizing data.
LANL-DW	Most accurate data computed by LANL codes. Same as LANL-PWB data set except DW calculations are used for collisional excitation and ionization data.
ADAS-NP	Most accurate data available in the ADAS database. Includes nonperturbative RMPS collisional excitation and TDCC and CCC collisional ionization data. The RMPS data are used for all transitions among spectroscopic levels of all ion stages. Spectroscopic levels include up to $n=4$ for the Li and Li^+ ion stages and up to $n=5$ for the Li^{2+} stage. The TDCC and CCC data are used for ionization from the neutral stage only, for levels up to $n=3$. Exchange classical impact parameter ionization data are used for the $n=4$ levels of the neutral stage. Distorted-wave data are used for ionization from the spectroscopic levels of the Li^+ and Li^{2+} ion stages. Distorted-wave data are used for dielectronic rates and a Gaunt factor approach used for the radiative recombination rates. Data for higher-lying levels, up to $n=500$, in all ion stages are provided by the projection matrix using more approximate results.

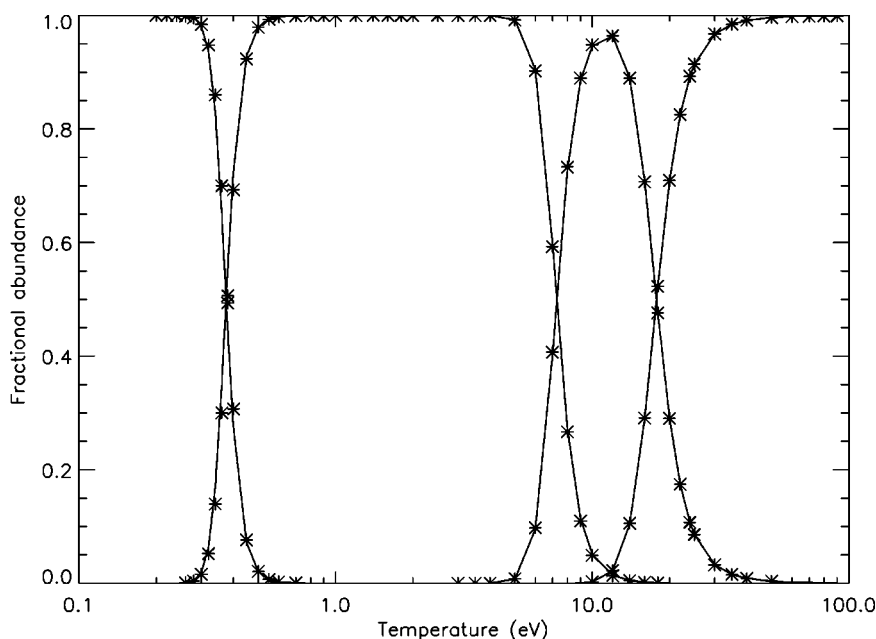


FIG. 1. Ionization balance at $N_e=10^{14} \text{ cm}^{-3}$ for the ADAS-1 and LANL-1 calculations. The solid curve shows the ADAS-1 results and the stars show the LANL-1 results. Note that the peak at lowest temperature corresponds to neutral lithium, the one centered at 2 eV is the He-like stage, the one at about 10 eV is the H-like stage, and the last peak is the bare nucleus.

III. RESULTS

To investigate the sensitivity of derived lithium plasma quantities to the underlying atomic data we calculated the ionization balance and radiated power loss with a range of atomic data sets (see Table II). Of particular interest is the sensitivity of these plasma quantities to the underlying collisional ionization and excitation rate coefficients. To make the comparison of the two codes meaningful various additional assumptions are made. First, it is assumed that the plasma is optically thin. Second, as mentioned earlier, it is assumed that the plasma is in steady state (i.e., the full equilibrium solution). Also, some checks were performed using the LANL-1 and ADAS-1 calculations to ensure that the LANL and ADAS codes were performing equivalent collisional-radiative calculations. The parameter space that was investigated encompassed $0.2 \text{ eV} \leq T_e \leq 90 \text{ eV}$ to allow for the presence of all ionization stages and $10^{10} \text{ cm}^{-3} \leq N_e \leq 10^{14} \text{ cm}^{-3}$ to study the effects of electron density.

A. Comparison of LANL and ADAS codes

Before going into the details of the collisional-radiative results, it was necessary to identify the regimes for which the LANL and ADAS codes were solving the collisional-radiative equations in an equivalent manner. As previously described, the two codes take differing approaches to solving the collisional-radiative equations and have access to different fundamental atomic data. Thus we carried out ADAS-1 calculations, which use LANL-DW data, to compare with LANL-1 calculations, also using LANL-DW data.

Ionization balance and radiated power loss calculations were performed using the two codes for the electron densities $N_e=10^{10} \text{ cm}^{-3}$, 10^{12} cm^{-3} , and 10^{14} cm^{-3} . The ionization balance data were found to agree extremely well for all three densities, and results for the highest density are displayed in Fig. 1. Similar excellent agreement was found for the radiated power loss data except at $N_e=10^{14} \text{ cm}^{-3}$ in the tempera-

ture range $1.0 \text{ eV} \leq T_e \leq 4.0 \text{ eV}$ where there is a maximum discrepancy of $\sim 10\%$, as displayed in Fig. 2. This plot clearly displays the radiation peaks from the neutral stage (at $T_e=0.4 \text{ eV}$), the He-like stage (at $T_e=8 \text{ eV}$), and the H-like stage (at $T_e=18 \text{ eV}$). In the $1.0 \text{ eV} \leq T_e \leq 4.0 \text{ eV}$ region the radiation is being emitted from the neutral stage, even though it makes up only a very small fraction of the total amount of ions (see Fig. 1). A closer examination of the neutral lithium ion fraction in this region shows that the ADAS-1 and LANL-1 results begin to separate at $T_e=1.0 \text{ eV}$. This is not surprising as it is well known that the levels arising from the $1s^2 2p$ configuration of Li-like ions can have populations comparable to the $1s^2 2s$ ground state. Consequently we note that, in this region, in order to model the neutral lithium emission accurately one must include the $1s^2 2p$ levels as being metastable in modeling codes such as ADAS, which assume that the majority of the population is held in the ground and metastable set of levels. However, this region, where the $1s^2 2p$ population becomes comparable to that of the ground state, is not one of the regimes that was chosen in this paper to track the sensitivities to underlying atomic data. Because of this choice and the fact that, as will be shown later, the bound-free emission from neutral lithium dominates the bound-bound radiation in this region, for the purposes of this study we do not consider the $1s^2 2p$ to be metastable in the ADAS modeling.

Outside of this temperature range the two approaches appear to produce equivalent calculations for $N_e=10^{14} \text{ cm}^{-3}$, as well as over the entire temperature range for $N_e=10^{10} \text{ cm}^{-3}$ and 10^{12} cm^{-3} , which allows us to draw conclusions related specifically to differences in the fundamental atomic data used in the detailed calculations of the next section. Also of note is that this good agreement was obtained despite the fact that ADAS ignored ionization to, and recombination from, excited levels. This observation provides support for the validity of this approximation at the low densities presently under consideration.

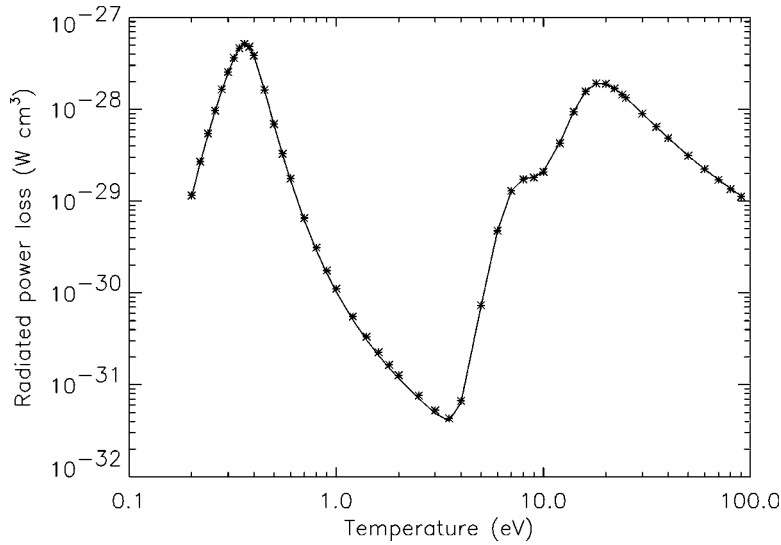


FIG. 2. Radiated power loss comparison at $N_e = 10^{14} \text{ cm}^{-3}$. The solid line shows the ADAS-1 results and the stars show the LANL-1 results.

Before leaving this discussion of the ADAS-1 and LANL-1 calculations it is instructive to analyze the effective ionization and recombination rate coefficients that are used by ADAS to obtain the ionization balance in Eq. (11). This analysis will highlight some differences in the ADAS and LANL approaches that will be helpful in understanding the detailed calculations of the following section. A comparison of these effective rate coefficients also provides an additional check that the ADAS-1 and LANL-1 calculations are equivalent.

In order to simplify this discussion we consider the ionization balance of the neutral lithium stage (labeled z), so that recombination from, and ionization to, the adjacent $z-1$ stage can be ignored in Eq. (5). Furthermore, we consider only a single metastable level (i.e., the ground state) to be defined for neutral lithium and the He-like ($z+1$) stage. Use of a single metastable for the neutral stage eliminates the Q and X cross-coupling coefficients. Also, the index σ unambiguously represents the lithium ground state. Similarly ν represents the He-like ground state and the summations over ν collapse to a single value. Combining these considerations with the steady-state condition transforms Eq. (5) into

$$\frac{dN_\sigma^z}{dt} = 0 = -S_{\sigma \rightarrow \nu} N_\sigma^z N_e + \alpha_{\nu \rightarrow \sigma} N_\nu^{z+1} N_e \quad (13)$$

$$\Rightarrow N_\sigma^z / N_\nu^{z+1} = \alpha_{\nu \rightarrow \sigma} / S_{\sigma \rightarrow \nu}. \quad (14)$$

Assuming that only neutral and He-like lithium are present (which is valid over a wide range of temperatures, due to the relative stability of the He-like ground state) the particle conservation boundary condition can be written

$$N_{\text{tot}} = N_\sigma^z + N_\nu^{z+1}. \quad (15)$$

Combining Eqs. (14) and (15) yields the ratios

$$\frac{N_\sigma^z}{N_{\text{tot}}} = \left(1 + \frac{S_{\sigma \rightarrow \nu}}{\alpha_{\nu \rightarrow \sigma}}\right)^{-1}, \quad \frac{N_\nu^{z+1}}{N_{\text{tot}}} = \left(1 + \frac{\alpha_{\nu \rightarrow \sigma}}{S_{\sigma \rightarrow \nu}}\right)^{-1}, \quad (16)$$

and so the fractional abundance of neutral and He-like lithium is completely determined from knowledge of the S and α effective rate coefficients.

To illustrate this last result we present Fig. 3. The solid lines represent the effective ionization and recombination rate coefficients in the above equation. The intersection of

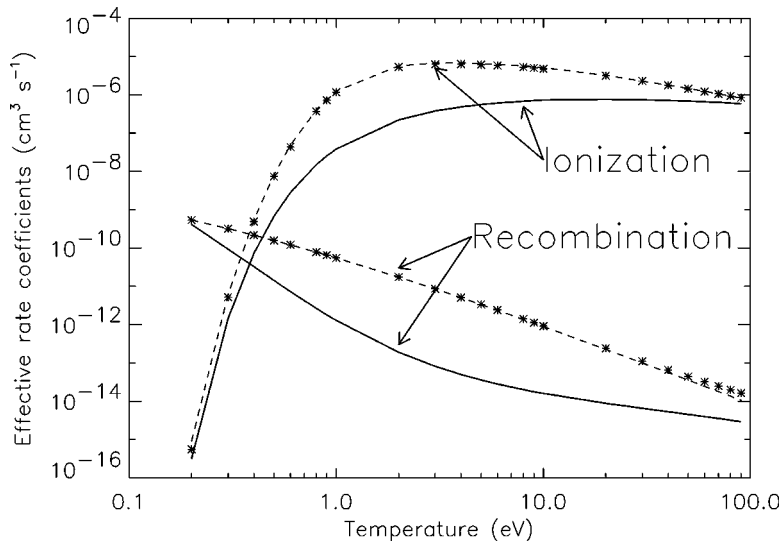


FIG. 3. Effective ionization and recombination rate coefficients at $N_e = 10^{14} \text{ cm}^{-3}$. The solid lines show the ADAS-1 (metastable resolved) effective rate coefficients, the dashed lines show the ADAS-1 (unresolved) effective rate coefficients, and the stars show the LANL-1 (unresolved) results.

these two curves, at roughly 0.4 eV, indicates the temperature at which there exist equal amounts of neutral and He-like lithium, which is consistent with the results presented in Fig. 1.

Although the LANL codes do not use effective ionization and recombination rate coefficients to determine ionization balance, it is possible to extract such quantities after the populations have been obtained from a solution of the collisional-radiative equations. In this case, since the LANL codes do not discriminate between metastable and excited levels, we consider the unresolved effective rate coefficients used in Eq. (2). These are to be distinguished from the metastable *resolved* coefficients that are used by ADAS in the metastable resolved picture and that appear in Eqs. (6) and (7). The unresolved effective rate coefficients for recombination into ion stage z and ionization out of ion stage z are determined from level populations and rate coefficients according to Eqs. (3) and (4).

The LANL values for these unresolved coefficients are represented as stars in Fig. 3. Note that the unresolved LANL data are considerably different from the ADAS metastable resolved coefficients, and yet both calculations produce the same ionization balance, as displayed in Fig. 1. In order to perform a meaningful comparison of the effective rate coefficients between the LANL-1 and ADAS-1 calculations, it is useful to compute the unresolved coefficients via Eqs. (3) and (4) within the ADAS-1 calculation, after the level populations have been obtained, and then to compare those values directly with the LANL-1 results.

The reader is reminded that the \mathcal{R} and \mathcal{S} rate coefficients are fundamental atomic data. They are computed by performing a Maxwellian average of the basic cross sections. Because the \mathcal{R} and \mathcal{S} rate coefficient values are identical in the two calculations, any difference in the *unresolved effective* rate coefficients displayed in Eqs. (3) and (4) points to a discrepancy in the populations. Furthermore, the unresolved coefficients often contain significant contributions from *high-lying* levels, providing a complementary diagnostic to the radiated power loss. This latter quantity is typically dominated by contributions from only a few low-lying levels at the low electron densities being considered in this work. The effective ionization rate coefficient, on the other hand, contains progressively more contributions from excited states as the density increases. To this end we have included in Fig. 3 the ADAS-1 values for the unresolved coefficients. The agreement is excellent for both the ionization and recombination coefficients.

B. Effects of atomic data on ionization balance

Given that the LANL-1 and ADAS-1 calculations produce almost identical results when using the same atomic data and size of model, it was decided to proceed with the more physically meaningful LANL-2 and ADAS-2 calculations. The most interesting question was to decide which data sets from Table II should be used in each code. Certainly it was desirable to compare the most accurate calculation from each code. Therefore a LANL-2 calculation using the LANL-DW data was performed, along with an ADAS-2 calculation us-

ing the ADAS-NP data. This ADAS-NP ionization balance calculation was run with nonperturbative TDCC and CCC electron impact ionization data for ionization from the neutral stage. These data include collisional ionization from all levels up through the $3d$ subshell. Distorted-wave ionization data were used for all spectroscopic (i.e., nonprojection matrix) levels of the He-like and H-like stages. It should be noted that the TDCC and CCC [9,10,21,22] ionization cross sections from the ground states of these two ion stages agree well with the corresponding distorted-wave data. However, there are currently no available TDCC and CCC ionization data from other levels of these two ion stages of lithium. R -matrix with pseudostate data were used in computing the electron impact excitation rate coefficients [6–8], while distorted-wave data were used to compute the dielectronic [11] rate coefficients and the radiative recombination rate coefficients were calculated using a Gaunt factor approach as outlined in [23]. The LANL-DW calculation included levels up to $n=8$ and distorted-wave data were used for all relevant processes. It was also decided to perform a LANL-2 calculation with the less accurate LANL-PWB data to determine how well such approximate results agree with the more accurate models.

Figure 4 shows the ion fractional abundances from our ADAS-2, ADAS-NP and LANL-2, LANL-DW calculations. One can see significant differences between the ADAS and LANL results in the $\text{Li} \rightarrow \text{Li}^+$ transitional region for the lower densities. There is a general improvement in the agreement for this transitional region as the density increases, until by $N_e=10^{14} \text{ cm}^{-3}$ there is very little difference between the various results. Above $T_e=5 \text{ eV}$, where the neutral stage is no longer dominant, the agreement between ADAS and LANL is quite good at all densities. This agreement is due in part to the fact that the ADAS-NP ionization data are in good agreement with the DW data for the charged stages of lithium. Also the LANL-DW and LANL-PWB calculations are in close agreement over the entire range of temperatures and densities, showing that the scaled hydrogenic results of Clark and Sampson [17] do a reasonably good job of predicting the DW results.

The reason for the differences in the neutral abundance at lower densities becomes apparent if one looks at the effective metastable resolved ionization coefficients produced by the ADAS code at $N_e=10^{10} \text{ cm}^{-3}$ (see Fig. 5). Initially it was thought that the differences in the ionization balance arose from large differences in the ADAS-NP (TDCC) versus LANL-DW ionization cross sections for the low-lying levels of neutral lithium (see the work of Colgan *et al.* [21]). However, Fig. 5 clearly displays that there is a dominant (order of magnitude) contribution to the ADAS ionization rate coefficient from highly excited states in the region of $T_e=0.4 \text{ eV}$, while the LANL result (not shown) contains only about a 25% excited-state contribution. In the case of the ADAS calculation, this contribution arises mostly from the projection matrix—i.e., from $1s^2nl$ where $5 < n \leq 500$. The LANL calculation, on the other hand, only includes levels up through $n=8$. A detailed study of the LANL calculation showed that the contributions to the effective ionization rate coefficient initially *decrease* with increasing n (contributing less than the ground state), but eventually turn around and increase

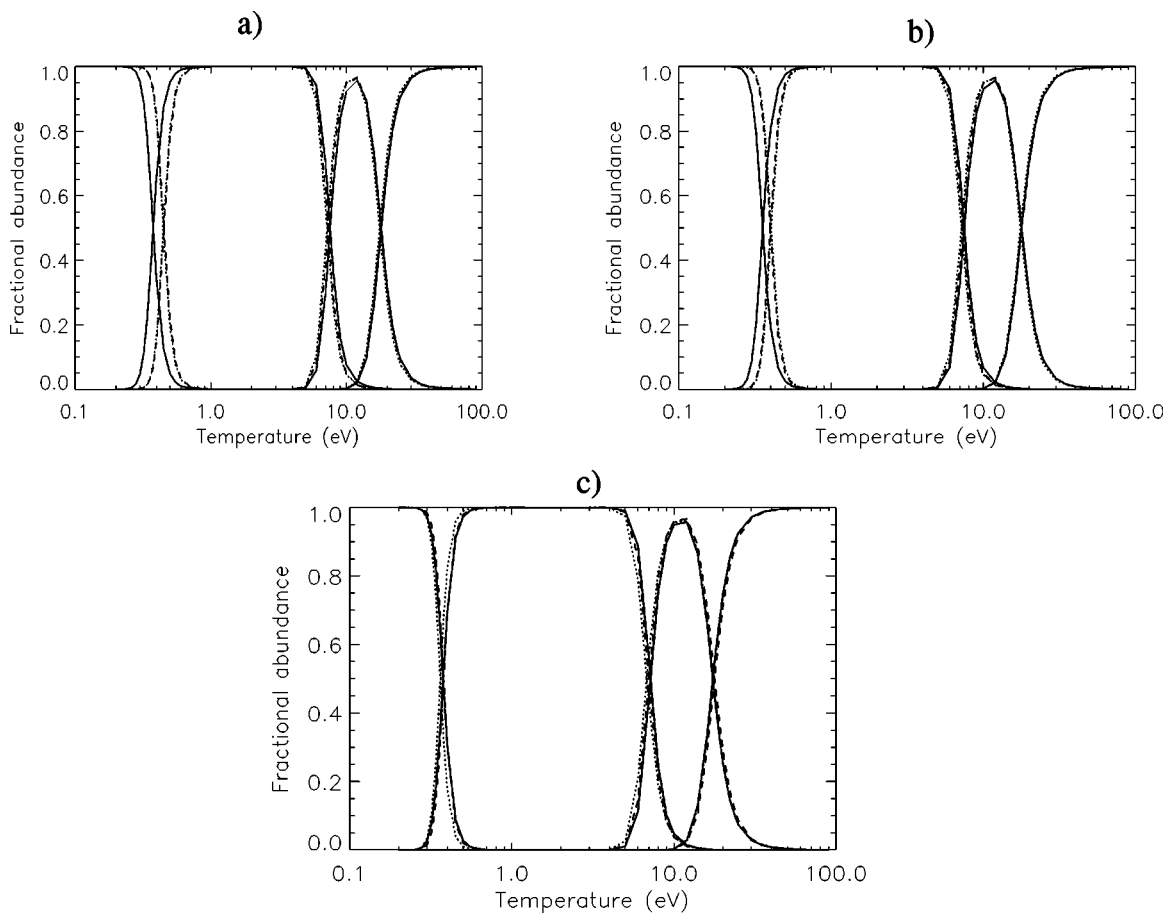


FIG. 4. Ionization balance at $N_e =$ (a) 10^{10} , (b) 10^{12} , and (c) 10^{14} cm^{-3} . The solid lines show the ADAS results, the dashed lines show the LANL-DW results, and the dotted lines show the LANL-PWB results.

toward the ground-state result. However, the highest $n=8$ level contribution is about one order of magnitude smaller than that of the ground state. Pushing the LANL calculation to $n=10$ shows individual level contributions that are still a factor of 2 smaller than the ground-state contribution. Presumably, if the LANL calculation could be extended to $n=100$, the effective ionization curves would show improved agreement.

The insensitivity of the neutral lithium ionization balance to the atomic data at higher densities was surprising at first. Once again Fig. 5 clearly displays a sizable contribution from the projection matrix to the ADAS effective ionization rate coefficients at $N_e=10^{14}$ cm^{-3} , and yet the ADAS and LANL ionization balance curves for the neutral stage in Fig. 4 are very similar. However, at this increased density, it turns out that the corresponding (resolved) ADAS and (unresolved) LANL effective recombination rate coefficients (not shown) also differ significantly, in such a way that the two codes provide very similar ionization balance data for the neutral stage at this density. This situation is reminiscent of the behavior observed in Fig. 3. The LANL unresolved data differed considerably from the ADAS resolved data, and yet the ionization balance results between the two calculations were identical. In the present case, however, we are not using identical data sets in the two codes. So what is the reason for this agreement?

In fact, the reason for this good agreement is physical in nature and can be attributed to the neutral stage being driven close to (collision-dominated) local thermodynamic equilibrium (LTE) conditions. This situation is demonstrated by the ionization balance plot in Fig. 6. It is evident that the neutral lithium ionization balance can be described by an LTE treatment at $N_e=10^{14}$ cm^{-3} , while the charged ion stages cannot.

Looking in more detail, one can see from Fig. 5 that as the density increases, even more of the effective ionization rate coefficient is made up of ionization from the highly excited states. Furthermore, as the electron density increases, progressively more of these excited populations are driven closer to their LTE value, which is consistent with the Byron boundary condition [12,24] extending down to lower- n shells. Thus, in both the ADAS and LANL calculations, the populations that are controlling the ionization balance are in LTE, and the main ionization mechanism is collisional ionization. As N_e increases the dominant recombination mechanism shifts from radiative recombination at $N_e=10^{10}$ cm^{-3} to three-body recombination at $N_e=10^{14}$ cm^{-3} . Since three-body recombination is computed via detailed balance from the collisional ionization data, the ionization balance is essentially insensitive to what ionization and recombination data are used. As long as the high-lying levels are in LTE and the three-body rates are computed consistently from the corresponding collisional ionization rates, the ionization balance

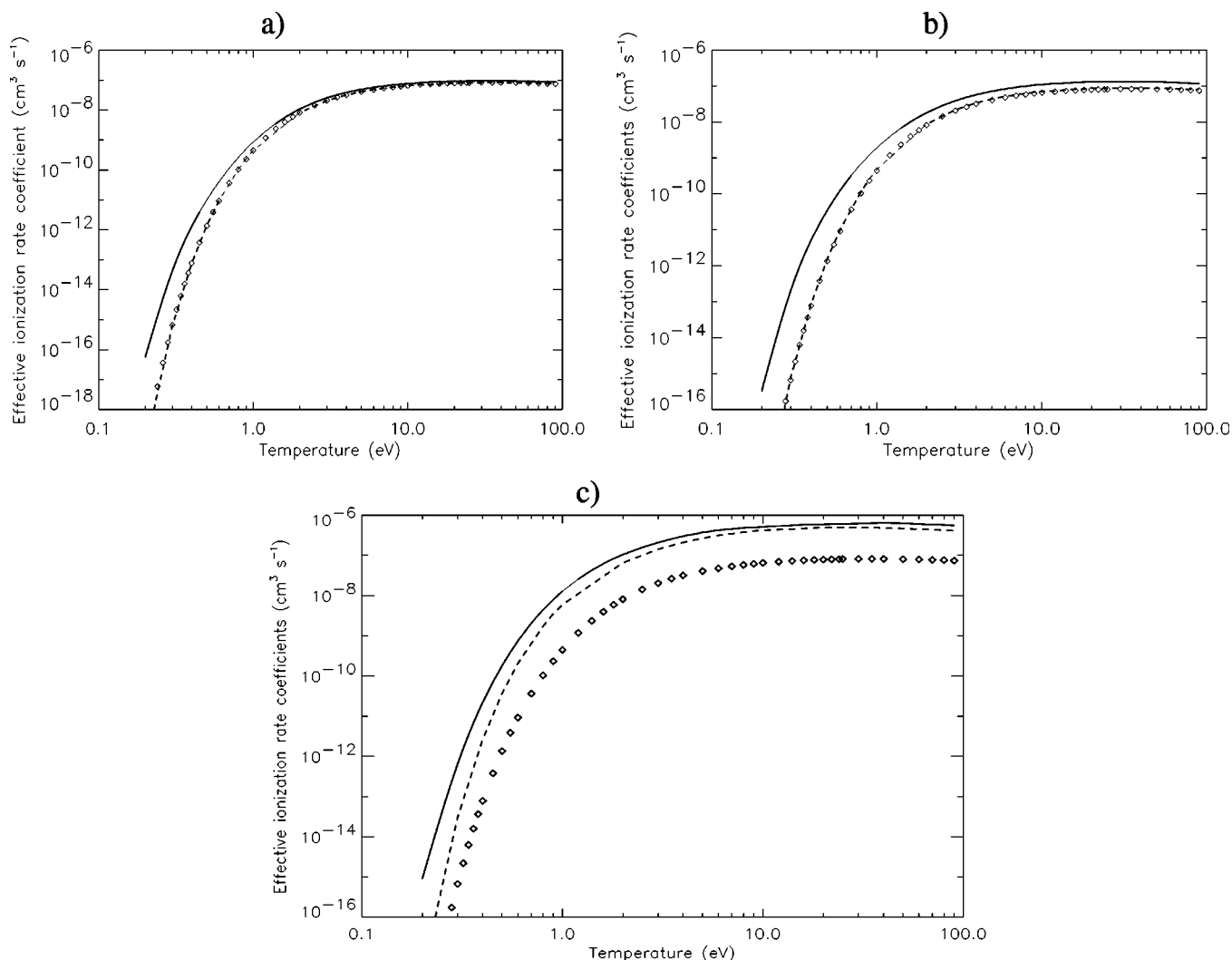


FIG. 5. ADAS-NP effective metastable resolved ionization rate coefficients for lithium at $N_e =$ (a) 10^{10} , (b) 10^{12} , and (c) 10^{14} cm^{-3} . The solid lines represent the ADAS-NP effective ionization rate coefficient (including contributions from the projection matrix), the dashed lines display the contribution from all spectroscopic levels (through the $n=4$ shell), and the diamonds display the contribution from the ground level only.

will remain unchanged. Thus for $N_e = 10^{14} \text{ cm}^{-3}$ we have a situation where the ionization balance of the neutral stage is controlled solely by ionization and recombination between the few highest-lying levels in that stage and the ground state of the He-like stage.

Based on this analysis, it appears that the neutral lithium ionization balance calculations for $N_e \geq 10^{14} \text{ cm}^{-3}$ will be relatively insensitive to the fundamental atomic data. Below this density the neutral stage ionization balance is dominated by collisional ionization from high-lying levels and a combination of radiative and three-body recombination from the He-like ground state. As mentioned previously, only perturbative data are available for collisional ionization from such high-lying levels. In light of these facts, nonperturbative studies are in progress to determine the accuracy of such data for $N_e < 10^{14} \text{ cm}^{-3}$.

For the He-like and H-like ion stages, the fractional abundance results of the three calculations are in good agreement. This is not altogether surprising since two of the data sets

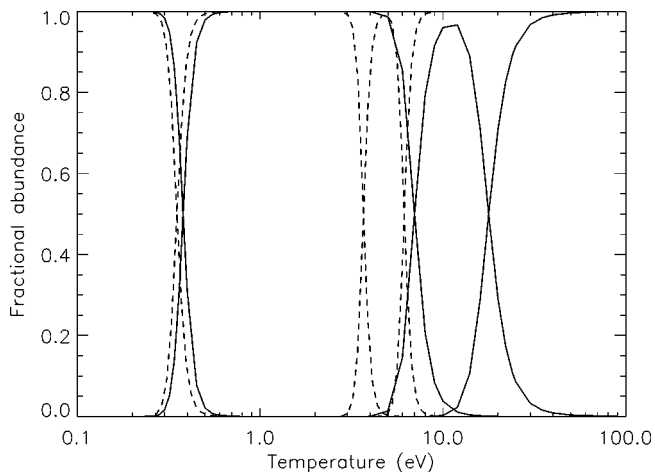


FIG. 6. LANL-DW ionization balance data at $N_e = 10^{14} \text{ cm}^{-3}$. The solid line shows non-LTE results. The dashed line shows the LTE results.

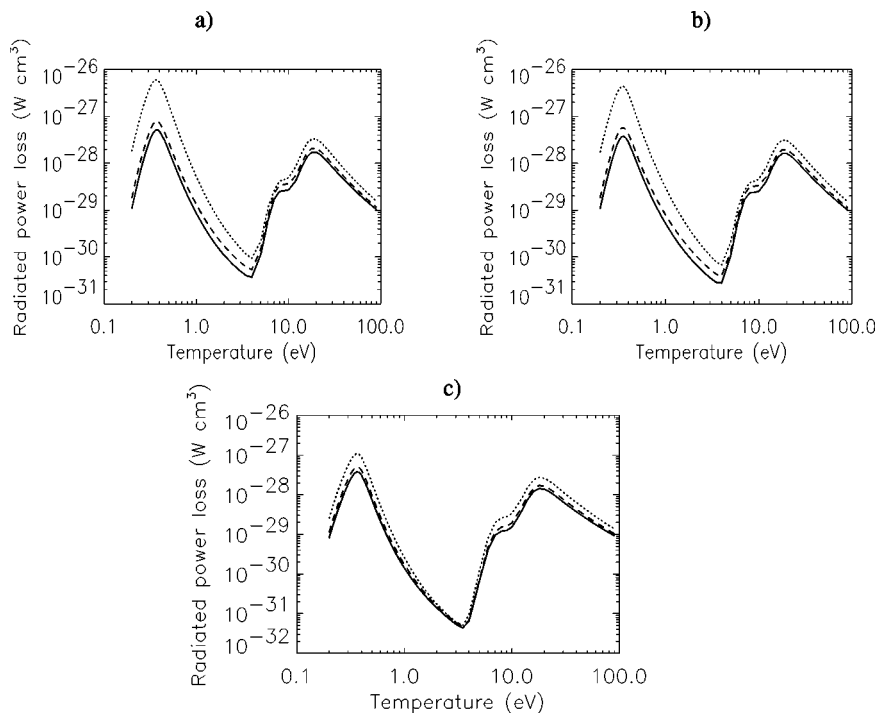


FIG. 7. Three ADAS-2 radiated power loss calculations using the same ADAS-NP ionization balance, but different excitation data sets. Results are provided for $N_e =$ (a) 10^{10} , (b) 10^{12} , and (c) 10^{14} cm^{-3} . The solid lines give the ADAS-NP results, the dashed lines give the LANL-DW results, and the dotted lines give the LANL-PWB results.

(ADAS-NP and LANL-DW) contain distorted-wave data and the third (LANL-PWB) contains analytic fits to distorted-wave data. It is known that the perturbative ground-state ionization cross section for each of these ion stages agrees well with nonperturbative data [10,25]. However, in light of recent work on nonperturbative calculations involving excitation to excited states [26] it is possible that distorted-wave ionization rate coefficients from excited states will, in fact, not agree with nonperturbative rate coefficients. Therefore it is useful to examine the contributions of the excited states to the effective ionization for the H-like and He-like ion stages to determine if using nonperturbative data could make a difference. Looking at the contribution to the ADAS effective ionization rate coefficients, one sees that for the H-like stage the effective ionization rate coefficient mostly consists of ionization from the ground state at the lower density. At the highest density of this study, the ground state makes up 65% of the total effective ionization, with the remainder coming from the projection matrix.

For the ADAS He-like stage, ionization from excited states is always significant. At $N_e = 10^{10} \text{ cm}^{-3}$ only 17% of the effective ionization comes from the ground, with 74% coming from the $1s2s \ ^3S$ metastable term. The remaining 9% comes from the projection matrix. For $N_e = 10^{14} \text{ cm}^{-3}$ only 8% comes from the ground, with 13% from the $1s2s \ ^3S$ term. The projection matrix makes up 26% of the total, with the remaining contribution coming from the other terms lying above the $1s2s \ ^3S$ term and below the start of the projection matrix at the $1s5s$ configuration.

Because so much of the effective ionization rate coefficient is made up of ionization from the $1s2s \ ^3S$ term, especially at the lower densities investigated, replacing the existing data with nonperturbative data could make a significant difference. We intend as a future study to use nonperturbative ionization data for these transitions in order to determine

whether the effective ionization rate coefficients, and resulting ionization balance, are affected. In a similar way, since ionization from excited states is also important for the H-like stage at the highest density, it would be interesting to study the effects of nonperturbative ionization from the excited states of that ion stage.

C. Effects of atomic data on radiated power loss

Before comparing the best possible ADAS and LANL radiated power loss results we provide an analysis of a useful hybrid calculation that underscores the sensitivity of these spectra to the excitation data. Consider the radiated power loss plots shown in Fig. 7. This figure shows three radiated power loss calculations, which differ only in the excitation data they use. We performed a hybrid calculation that combined ADAS-2-type calculations with LANL data. In particular we recalculated the ADAS-2 excited-level populations, Eq. (10), using excitation data from the LANL-PWB and LANL-DW data sets in place of the RMPS data, but retained the ADAS-2/ADAS-NP metastable populations (i.e., ionization balance) from the steady-state solution of Eq. (5). The same projection matrix data were used in each case. Thus the three different excitation data sets were *R*-matrix with pseudostates (labeled ADAS-NP in the figure), LANL distorted-wave (labeled LANL-DW), and LANL plane-wave Born (labeled LANL-PWB) sets.

It is instructive to connect the differences in the radiated power loss to specific differences in the effective collision strengths for each ion stage. Table III gives the percentage differences at the temperatures for the peak emission regions for the Li-like (0.36 eV), He-like (8 eV), and H-like (18 eV) ion stages.

For neutral lithium the dominant emission at 0.36 eV comes from the $1s^2 2p \ ^2P \rightarrow 1s^2 2s \ ^2S$ spectral line, with the

TABLE III. Factor differences in the radiated power loss for the ADAS calculations using LANL-DW, LANL-PWB, and ADAS-NP excitation data, corresponding to Fig. 7.

T_e (eV)	$N_e=10^{10}$ cm $^{-3}$		$N_e=10^{12}$ cm $^{-3}$		$N_e=10^{14}$ cm $^{-3}$	
	PWB/ADAS	DW/ADAS	PWB/ADAS	DW/ADAS	PWB/ADAS	DW/ADAS
0.36	11.91	1.53	11.43	1.53	2.91	1.33
8.00	1.64	1.35	1.65	1.34	2.18	1.27
18.00	1.93	1.20	1.92	1.20	1.92	1.19

$1s^22p\ ^2P$ term being populated overwhelmingly due to excitation from the ground state. In a case such as this, according to Eq. (12) the ratio of the radiated power loss values given in Table III can be well approximated by the ratio for the two calculations of the product of the A value times the energy of the transition times the effective collision strength for the dominant populating pathway. The A values for $1s^22p\ ^2P \rightarrow 1s^22s\ ^2S$ differ by 6% for the different data sets, and the energies are within 2%. Thus the difference in the radiated power loss for neutral lithium given in Table III, for both the LANL-DW and LANL-PWB cases, is due almost completely to the difference in the effective collision strength of the $1s^22s\ ^2S \rightarrow 1s^22p\ ^2P$ transition. We note that continuum coupling effects for this transition are small and that the majority of the difference between the distorted-wave and RMPS rate coefficients is due to the differences in the threshold behavior of the two calculations.

For the He-like lithium case the situation is more complex. For the ADAS-NP and LANL-DW cases the radiated power loss is made up almost equally between emission from the $1s2p\ ^1P \rightarrow 1s^2\ ^1S$ and $1s2p\ ^3P \rightarrow 1s2s\ ^3S$ transitions. Both of these excited terms are populated via more than just excitation directly from the ground term, with stepwise excitation via the $1s2s\ ^1S$, $1s2s\ ^3S$, and $1s2p\ ^3P$ terms all being significant. Of the main excitation transitions which populate the $1s2p\ ^1P$ and 3P terms the LANL-DW effective collision strengths range from a factor of 1.2 to a factor of 2.0 higher than the ADAS-NP excitation data, resulting in a radiated power loss which is about a factor of 1.27–1.35 higher than the ADAS-NP radiated power loss.

It is rather surprising that the He-like LANL-PWB excitation data produce a radiated power loss which is a only factor of 1.64–2.18 greater than the ADAS-NP excitation data results. All of the LANL-PWB excitation effective collision strengths are greater than the ADAS-NP data by about a factor of 10, and there are no spin changing transitions in the LANL-PWB data set. The combination of the fact that the LANL-PWB excitation effective collision strengths are all higher than ADAS-NP and the fact that one has less routes to populate the excited states, due to the lack of spin changing transitions, leads to a LANL-PWB radiated power loss which is within a factor of 2.2 of the ADAS-NP results. It is interesting to note that if spin changing transitions are inserted into the LANL-PWB datafile (even if it is RMPS spin changing data), then the radiated power loss for the He-like stage becomes about a factor of 10 greater than the ADAS-NP results, more consistent with the differences seen in the effective collision strengths. Thus the factor of 2 difference for the LANL-PWB is somewhat fortuitous.

For the H-like radiated power loss, the explanation is more straightforward. The dominant transition in radiated power loss is the $2p \rightarrow 1s$ transition, making up 90% of the radiation at all densities. The $n=2$ shell is populated predominantly via excitation from the ground state. Thus in this case virtually all of the difference observed in the radiated power loss when comparing the LANL-DW and LANL-PWB results with the ADAS-NP results is due to differences in the effective collision strengths for excitation from the $1s$ to $2p$ subshell.

Having isolated the differences in the radiated power loss due to differences in the effective collision strengths, the final study is to compare the most accurate ADAS calculations with the most accurate LANL calculations for the radiated power loss. Data are shown in Fig. 8 for the ADAS-2 calculations using ADAS-NP data and LANL-2 calculations using LANL-PWB and LANL-DW data. Table IV gives the percentage differences in the radiated power loss results at the peak emission temperatures for each of the ion stages.

Noting the similarities between Figs. 7 and 8 one can see that much of the difference in the radiated power loss data obtained from the most accurate ADAS and LANL calculations can also be explained in terms of differences in the excitation data used in the two models. In general the LANL results lie higher than the ADAS ones, with better agreement being found for the He-like and H-like stages than for the neutral stage. Once again the LANL-PWB results are consistently higher than the LANL-DW results over the entire range of physical conditions.

Quantitatively, the LANL-DW radiated power loss calculations give a peak radiation from the neutral lithium stage (at $T_e=0.36$ eV) that is a factor of 2.25 and 2.56 greater than the ADAS results at the lower densities of $N_e=10^{10}$ and 10^{12} cm $^{-3}$, respectively. As was seen from Fig. 7, a factor of ~ 1.5 can be explained by taking into account the differences in the effective collision strength of the $1s^22s\ ^2S \rightarrow 1s^22p\ ^2P$ transition. The remaining differences in the radiated power loss are due largely to differences between the ADAS and LANL ionization balance results, as discussed in Sec. III B. These differences further enhance the LANL results and lead to a shift in the peak emission region of those data to higher temperatures. At the highest density the agreement is considerably better, but the LANL-DW peak is still a factor of 1.36 higher, with this difference being mainly due to differences in the aforementioned effective collision strength. The improvement at higher density is caused by the plasma being driven close to LTE for the neutral stage. However, the lowest-lying levels (especially the $1s^22p\ ^2P$ term, responsible for the bulk of the radiation) still retain some non-LTE character.

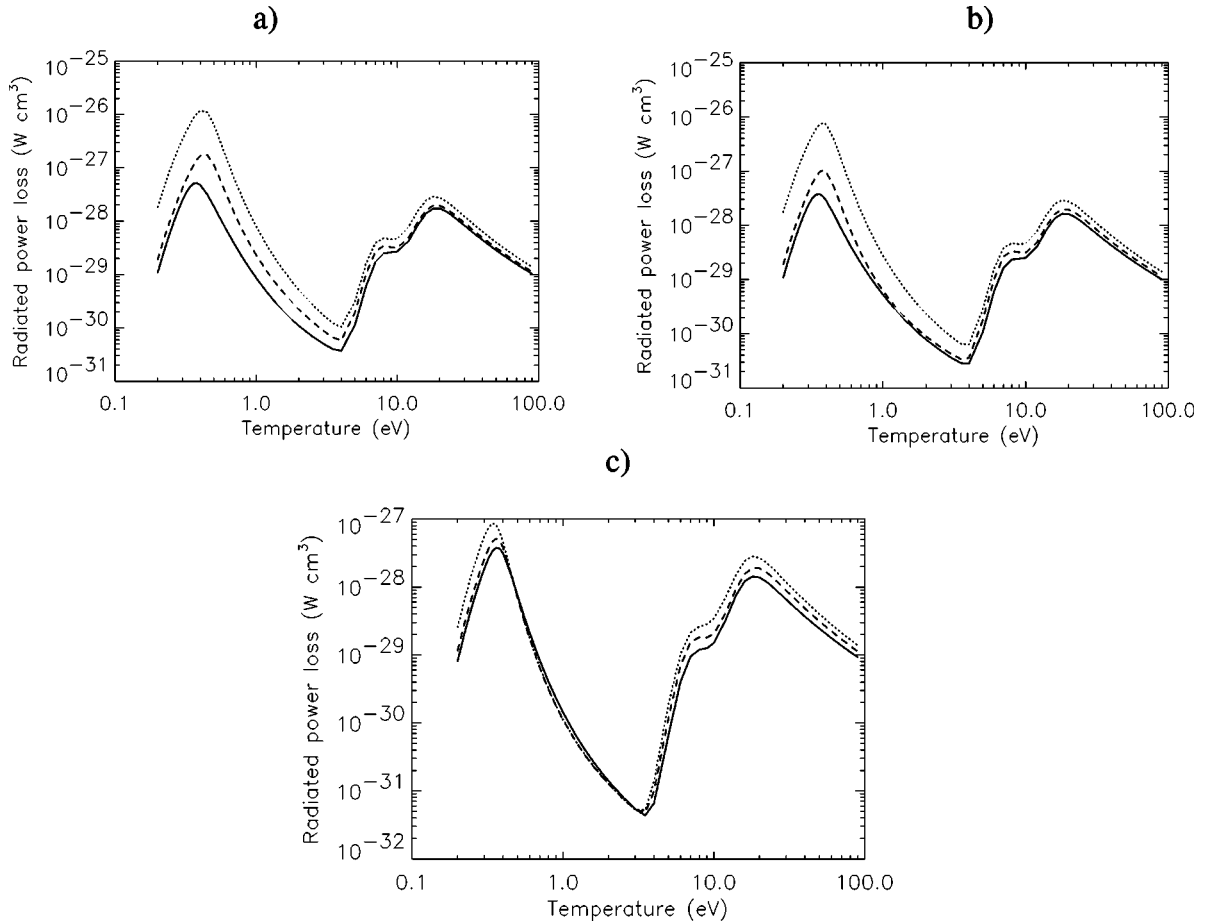


FIG. 8. Radiated power loss comparison at $N_e =$ (a) 10^{10} , (b) 10^{12} , and (c) 10^{14} cm^{-3} . The solid lines give the ADAS results, the dashed lines give the LANL-DW results, and the dotted lines give the LANL-PWB results.

As expected, the agreement between ADAS and LANL for radiation from the He-like and H-like stages is better than for radiation from the neutral stage. From comparisons of Tables III and IV it can be seen that the differences are roughly consistent with the differences in the effective collision strengths.

In detail, the LANL-DW He-like peak radiation (at $T_e = 8$ eV) is greater than the ADAS peak by a factor of 1.38–1.52 over the density range. Similarly the LANL-DW, H-like peak radiation (at $T_e = 18$ eV) is greater than the ADAS peak by a factor of 1.14–1.34 over the density range. The general trend is for the He-like and H-like LANL-DW radiated power loss to agree less with the ADAS results as the electron density increases. This trend in density is clearly not a consequence of differences in the excitation data, since Table

III showed no such trend in the radiated power loss ratios. Instead this enhanced discrepancy with increasing density is due to differences in the ratio of the fractional abundances (i.e., ionization balance) of the LANL to ADAS results increasing with density. Although the trend with density is caused by the fractional abundance differences, most of the difference between the LANL and ADAS radiated power loss results is caused by the excitation data. While conventional wisdom might have predicted better agreement between DW and RMPS radiated power loss results for these charged stages, recent work [7,8] has shown that the DW excitation cross sections among the low-lying levels of these lithium ion stages can be too high by $\sim 25\%$ at threshold. As mentioned earlier in this section, in connection with the neutral ion stage, these differences are due to the threshold be-

TABLE IV. Factor differences in the radiated power loss for the LANL-2 and ADAS-2 calculations that are presented in Fig. 8.

T_e (eV)	$N_e = 10^{10} \text{ cm}^{-3}$		$N_e = 10^{12} \text{ cm}^{-3}$		$N_e = 10^{14} \text{ cm}^{-3}$	
	PWB/ADAS	DW/ADAS	PWB/ADAS	DW/ADAS	PWB/ADAS	DW/ADAS
0.36	17.04	2.25	19.27	2.56	2.18	1.36
8.00	1.91	1.38	1.99	1.44	2.18	1.52
18.00	1.67	1.14	1.77	1.21	1.97	1.34

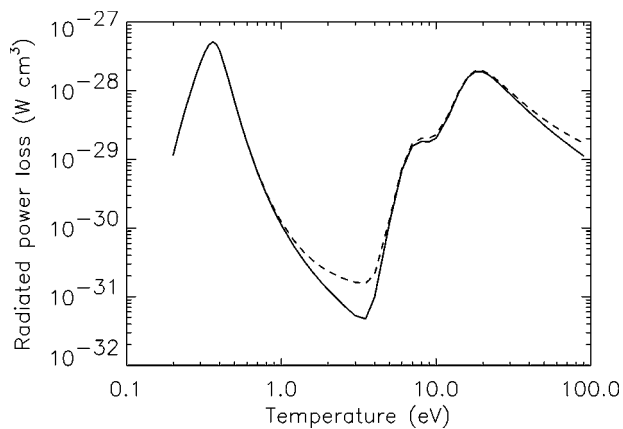


FIG. 9. Radiated power loss showing the bound-free contribution at $N_e=10^{14} \text{ cm}^{-3}$. The solid line shows the LANL-DW result that uses only the bound-bound contribution. The dashed line contains both the bound-bound and bound-free contributions.

havior of the excitation cross sections rather than continuum coupling effects.

As a specific example, consider the relatively large factor of 1.34 difference in the H-like peak emission at the highest density, which was a bit surprising for a simple one-electron system. At these temperatures ($T_e \approx 18 \text{ eV}$) it was found that the LANL-DW effective collision strength from the ground state to the $2p$ configuration, from which most of the radiation is emitted, was $\sim 20\%$ greater than the ADAS-NP (RMPS) values. There is also a difference of $\sim 10\%$ in the LANL versus ADAS ionization balance at that temperature. These two discrepancies produce the majority of the factor difference seen in the radiated power loss. Note that at $T_e = 18 \text{ eV}$ the relevant H-like effective collision strengths (or excitation rate coefficients) are dominated by the threshold behavior of their corresponding cross sections. For example, the threshold energy for the $1s \rightarrow 2s$ transition is about 92 eV , which is about a factor of 5 greater than the electron temperature. Similar statements can be made concerning the ionization rate coefficients and their corresponding cross sections. Thus, it is apparently this dependence on the threshold behavior of the fundamental atomic data that causes the differences in the two models at $T_e = 18 \text{ eV}$. Note that in Fig. 8 the discrepancies in the radiated power loss consistently decrease as the temperature increases beyond 18 eV because the relevant (i.e., spectroscopic) level populations depend more on the fundamental cross section data away from threshold, where the data are expected to trend towards better agreement for a one-electron ion.

For completeness we mention here that the bound-free contribution (not included up to this point) to the radiated power loss at the highest density is becoming significant. The effect is displayed in Fig. 9 for $N_e=10^{14} \text{ cm}^{-3}$. While there are significant differences, the main point to be made is that these differences do not impact any of the main conclusions of this work. There is a significant increase in the radiated power loss in the temperature range $1 \text{ eV} < T_e < 4 \text{ eV}$, with a maximum increase of about a factor of 5. This is precisely the temperature/density range discussed earlier for which the single metastable picture was breaking down. Thus the pre-

viously discussed discrepancies in the bound-bound radiated power loss data, caused by the resolution of only a single metastable level, may in reality be unobservable when comparisons are made between complete radiated power loss calculations that include the bound-free contribution. For these plasma conditions this contribution simply overwhelms the bound-bound result. There is also a smaller, but significant, increase (almost a factor of 2) in the H-like emission due to the bound-free contribution at the highest temperatures. Thus our conclusions regarding the bound-free contribution is that it should be included in the radiated power loss calculations at the higher densities if accurate data are required for detailed comparisons.

Based on this overall radiated power loss analysis we conclude that nonperturbative, RMPS excitation data should be used in modeling the populations of all ion stages of lithium up to electron densities in the range of $N_e=10^{14} \text{ cm}^{-3}$. Even for the simplest Li^{2+} ion stage, for which modeling with perturbative data is often assumed to be sufficient, the RMPS excitation data were found to produce significant differences in the radiated spectra, in accordance with the issues discussed in [8].

IV. SUMMARY

Combining the ADAS and LANL approaches provides a powerful technique for testing the sensitivity of collisional-radiative modeling to various sets of atomic data. However, care must be taken when comparing two collisional-radiative codes which were designed for quite different purposes, such as the LANL and ADAS suites. If a regime is being studied for which either code was not designed, then either a meaningful comparison cannot be performed or, if possible, suitable code modifications must be applied in order to allow a comparison to be made. For example, if one were to study higher densities than those in this paper, then the ADAS codes would need to include a larger metastable set. This notion was, in fact, already observed in some of our highest-density results for neutral lithium at temperatures above 1 eV . On the other hand, nonperturbative data are not easily included in the LANL codes, and it would not be surprising to see significant differences for neutrals and near neutrals when comparing with results generated using nonperturbative data. This behavior was indeed found to be the case in this work, and it was this fact that allowed us to isolate some of the regimes for which nonperturbative data must be used.

For the radiated power loss it was found that the nonperturbative (RMPS) excitation data provided a measurable difference in this spectral quantity over the perturbative (DW) results. The application of RMPS excitation data to collisional-radiative modeling of other first-row elements should yield similar differences. In the case of lithium, differences in the radiated power loss were most notable for the neutral-stage emission at low densities, although a portion of this discrepancy is due to a difference in the ionization balance. The largest discrepancies are about a factor of 2.5 when comparing LANL distorted-wave calculations to those of ADAS. Agreement between the radiated power loss data for the neutral stage was significantly better at the highest

density and is expected to further improve with increasing density as LTE conditions prevail. Similar radiated power loss comparisons for the Li^+ and Li^{2+} ion stages showed discrepancies ranging from 10% to 50% in the peak ion stage emission, depending on density. For these two ion stages, the plasma remains in a collisional-radiative regime at the highest density, and differences between the perturbative and nonperturbative radiated power loss results are expected to persist to somewhat higher densities due to differences in the collisional excitation data sets. For all plasma conditions, the LANL-PWB excitation data provided radiated power loss results that were consistently higher than those obtained from the LANL-DW excitation data. This behavior resulted in more pronounced discrepancies between the PWB and nonperturbative spectra.

The evidence concerning the importance of nonperturbative, ionization data in collisional-radiative modeling of lithium remains inconclusive. For electron densities below 10^{14} cm^{-3} significant differences were observed for the ionization balance of the neutral stage, but this discrepancy appeared to be due to the inclusion of more high- n -level data in the ADAS calculations via the projection matrix, rather than due to a difference in the quality of the underlying data. For an electron density of 10^{14} cm^{-3} the neutral stage of the plasma is collision dominated and all but the lowest levels are populated according to LTE conditions. Therefore, the use of perturbative (DW or scaled-hydrogenic) ionization data was sufficient to produce reasonable agreement with nonperturbative models for the ionization balance of the neutral stage.

Good agreement was obtained between the ADAS and LANL calculations over the entire density range for the Li^+ and Li^{2+} ionization balance results because only (perturba-

tive) distorted-wave ionization data were used in all cases. The ground-state perturbative ionization cross sections used in this paper for Li^+ and Li^{2+} are, in good agreement with recent nonperturbative calculations. However, the role of nonperturbative data for ionization from the excited states could still be of interest. Perturbative data were used for all of the ionization data from excited states of Li^+ and Li^{2+} , and thus it was not possible to assess the role of nonperturbative data on these processes. Recent work suggests that perturbative ionization rate coefficients from excited states may differ significantly from nonperturbative data. Ionization from the $1s2s\ ^3S$ term would be particularly interesting to investigate. In general, access to perturbative ionization data from excited levels of Li^+ and Li^{2+} would provide additional insight into the importance of such data in collisional-radiative modeling.

Looking toward future research possibilities we point out that lithium is the simplest alkali metal, with a single valence electron outside of a closed shell. This electronic structure—and specifically the relative stability of the He-like ground state—is responsible for some of the collisional-radiative properties that were observed for the neutral ion stage. In the future, we hope to study more complex systems, such as beryllium, which contain a closed shell in the neutral stage and for which abundant data are available.

ACKNOWLEDGMENTS

This work was supported in part by a U.S. Department of Energy SciDAC grant (Grant No. DE-FG02-01ER54644) to Auburn University. One of us (C.J.F.) would like to thank J. Abdallah and R. E. H. Clark for discussions concerning the LANL codes.

-
- [1] http://www.cfadc.phy.ornl.gov/data_and_codes
- [2] H. Summers, ADAS Manual V2.6, <http://adas.phys.strath.ac.uk/>
- [3] <http://dbshino.nifs.ac.jp>, National institute for fusion science: Atomic and molecular database.
- [4] J. Abdallah, R. E. H. Clark, J. M. Peek, and C. J. Fontes, *J. Quant. Spectrosc. Radiat. Transf.* **51**, 1 (1994).
- [5] R. Brandenburg, J. Schweinzer, S. Fiedler, F. Aumayr, and H. P. Winter, *Plasma Phys. Controlled Fusion* **41**, 471 (1999).
- [6] D. C. Griffin, D. M. Mitnik, J. Colgan, and M. S. Pindzola, *Phys. Rev. A* **64**, 032718 (2001).
- [7] C. P. Ballance, N. R. Badnell, D. C. Griffin, S. D. Loch, and D. M. Mitnik, *J. Phys. B* **36**, 235 (2003).
- [8] C. P. Ballance, N. R. Badnell, and E. S. Smyth, *J. Phys. B* **36**, 3707 (2003).
- [9] J. Colgan, M. S. Pindzola, D. M. Mitnik, and D. C. Griffin, *Phys. Rev. A* **63**, 062709 (2001).
- [10] M. S. Pindzola, D. M. Mitnik, J. Colgan, and D. C. Griffin, *Phys. Rev. A* **61**, 052712 (2000).
- [11] N. R. Badnell, M. G. O'Mullane, H. P. Summers, Z. Altun, M. A. Bautista, J. Colgan, T. W. Gorczyca, D. M. Mitnik, M. S. Pindzola, and O. Zatsarinny, *Astron. Astrophys.* **406**, 1151 (2003).
- [12] T. Kawachi, T. Fujimoto, and G. Csanak, *Phys. Rev. E* **51**, 1428 (1995).
- [13] T. Kawachi and T. Fujimoto, *Phys. Rev. E* **51**, 1440 (1995).
- [14] T. Kawachi, *Phys. Rev. E* **67**, 016409 (2003).
- [15] J. Schweinzer, R. Brandenburg, I. Bray, R. Hoekstra, F. Aumayr, R. K. Janev, and H. P. Winter, *At. Data Nucl. Data Tables* **72**, 239 (1999).
- [16] H. P. Summers, JET joint undertaking report JET-IR(93)07, 1993 (unpublished).
- [17] R. E. H. Clark and D. H. Sampson, *J. Phys. B* **17**, 13311 (1984).
- [18] D. R. Bates, A. E. Kingston, and R. W. P. McWhirter, *Proc. R. Astron. Soc. London, Ser. A* **267**, 297 (1962).
- [19] A. Burgess and H. P. Summers, *Mon. Not. R. Astron. Soc.* **174**, 345 (1976).
- [20] V. L. Jacobs and J. Davis, *Phys. Rev. A* **18**, 697 (1978).
- [21] J. Colgan, M. S. Pindzola, D. M. Mitnik, D. C. Griffin, and I. Bray, *Phys. Rev. Lett.* **87**, 213201 (2001).
- [22] I. Bray and A. T. Stelbovics, *Phys. Rev. Lett.* **70**, 746 (1993).

- [23] H. P. Summers and M. B. Hooper, *Plasma Phys.* **25**, 1131 (1983).
- [24] S. Byron, R. C. Stabler, and P. I. Bortz, *Phys. Rev. Lett.* **8**, 376 (1962).
- [25] J. Colgan, M. S. Pindzola, and F. Robicheaux, *Phys. Rev. A* **66**, 012718 (2002).
- [26] M. Witthoef, J. Colgan, M. S. Pindzola, C. P. Ballance, and D. C. Griffin, *Phys. Rev. A* **68**, 022711 (2003).